Northumbria Research Link

Northumbria
University
NEWCASTLE

Enhanced electrochemical performance of $CuCo_2S_4$/carbon nanotubes composite as electrode material for supercapacitors

Hao Li[1], Zhijie Li[1*], Zhonglin Wu[1], Mengxuan Sun[1], Shaobo Han[2], Chao Cai[2], Wenzhong Shen[3], XiaoTeng Liu[4], YongQing Fu[4**]

[1]School of Physics, University of Electronic Science and Technology of China, Chengdu, 610054, P. R. China

[2]Institute of Fundamental and Frontier Sciences, University of Electronic Science and Technology of China, Chengdu, 610054, P. R. China

[3]State Key Laboratory of Coal Conversion, Institute of Coal Chemistry, Chinese Academy of Science, Taiyuan, 030001, China

[4]Faculty of Engineering and Environment, Northumbria University, Newcastle Upon Tyne, NE1 8ST, UK

Zhijie Li (**Corresponding Author**): ORCID: 0000-0001-9870-9939;

*E-mail: zhijieli@uestc.edu.cn; TEL: +86 02883202160

Richard YongQing Fu (**Corresponding Author**): ORCID: 0000-0001-9797-4036;

*E-mail: Richard.fu@northumbria.ac.uk; TEL: +44 (0)191 2274662

Abstract

$CuCo_2S_4$ is regarded as a promising electrode material for supercapacitor, but has inferior conductivity and poor cycle stability which restrict its wide-range applications. In this work, hierarchically hybrid composite of $CuCo_2S_4$/carbon nanotubes (CNTs) was synthesized using a facile hydrothermal and sulfuration process. The embedded CNTs in the $CuCo_2S_4$ matrix provided numerous effective paths for electron transfer and ion diffusion, and thus promoted the faradaic reactions of the $CuCo_2S_4$ electrode in the energy storage processes. The $CuCo_2S_4$/CNTs-3.2% electrode exhibited a significantly increased specific capacitance of 557.5 F g^{-1} compared with those of the pristine $CuCo_2S_4$ electrode (373.4 F g^{-1}) and CuO/Co_3O_4/CNTs-3.2% electrode (356.5 F g^{-1}) at a current density of 1 A g^{-1}. An asymmetric supercapacitor (ASC) was assembled using the $CuCo_2S_4$/CNTs-3.2% as the positive electrode and the active carbon as the negative electrode, which exhibited an energy density of 23.2 Wh kg^{-1} at a power density of 402.7 W kg^{-1}. Moreover, the residual specific capacitance of this ASC device retained 85.7 % of its original value after tested for 10000 cycles, indicating its excellent cycle stability.

Key words: $CuCo_2S_4$, CNTs, Composite, Electrochemical performance, Supercapacitor.

1. Introduction

Supercapacitor has received much attention in recent years owing to its short charge/discharge time, high power density, good cycle stability, low maintenance cost and environmental friendliness [1-3]. Many electrode materials including metal oxides/hydroxides [5, 6], metal sulfides [7], conductive polymers [8, 9] and carbon materials [4] have been investigated for the supercapacitors. Among them, the carbon materials exhibit low specific capacitances. Metal oxides/hydroxides generally have high theoretical capacitances, however the experimentally obtained capacitances are often much lower than their theoretical values [10]. In addition, many of these metal oxides/hydroxides exhibit poor rate capability. Transition-metal sulfides including Co_3S_4 [11, 12], Ni_3S_2 [13], MoS_2 [14, 15], CuS [16, 17] and ZnS [7] have been reported to achieve large specific capacitances and high rate capability due to their good electrical conductivity and high electrochemical activity, and thus have been considered as the promising electrode materials for supercapacitors. Among them, cobalt sulfides have been attracted much attention due to their high capacitance values and good stability. However, cobalt is relatively expensive and toxic, which limits its practical application as electrode materials. Therefore, binary metal sulfides of MCo_2S_4 (M = Ni, Zn, Cu, Mn and *etc*.) [18-21] have received increasing attention due to their low cost and low toxicity. However, the capability and stability of these MCo_2S_4 compounds need to be significantly enhanced.

One of the effective strategies to improve the specific capacitance and cycling stability of binary metal sulfides is to form hybrid structures with highly conductive

materials, such as carbon materials [22-24] and conducting polymer [10]. For examples, $CuCo_2S_4$/polyacrylonitrile exhibited a specific capacitance of 385 F g^{-1} at 1 A g^{-1} [25]. The polypyrrole/$NiCo_2S_4$ exhibited a specific capacitance of 911 F g^{-1} at 1 A g^{-1}, which is higher than that of pure $NiCo_2S_4$ (470 F g^{-1}) [10]. $NiCo_2S_4$/active carbon (AC) synthesized using a two-step hydrothermal method showed a specific capacitance of 605.2 F g^{-1} at 0.5 A g^{-1} [26]. Due to their good electrical conductivity, excellent mechanical property and chemical stability, carbon nanotubes are often regarded as one of the promising candidates to construct the hybrid architectures of MCo_2S_4/CNTs composites for improving their electrochemical performance. The one dimensional structure of CNTs provides effective paths for electron transfer and ion diffusion, thus effectively reducing the charge transfer resistance of the composite [27]. For example, Jin et al prepared CNTs/$CuCo_2S_4$ nanocrystallite composites using a solvothermal method, which exhibited an specific capacitance of 606 F g^{-1} at 1 A g^{-1} [28]. However, these composites showed a poor cycle stability in the long-term charge/discharge processes.

In this study, a hierarchically hybrid $CuCo_2S_4$/CNTs composite was prepared using a facile hydrothermal and sulfuration process, and then explored as a high-performance electrode material for supercapacitors. Firstly, Co_3O_4/CuO/CNTs composite was synthesized using a simple hydrothermal method, and then it was transformed into $CuCo_2S_4$/CNTs composite *via* a sulfuration process. Due to the reduced series resistance and charge transfer resistance, the $CuCo_2S_4$/CNTs electrode showed a higher specific capacitance than those of the pristine $CuCo_2S_4$ and the Co_3O_4/CuO /CNTs

electrodes. Moreover, an asymmetrical supercapacitor (ASC) was assembled using $CuCo_2S_4$/CNTs-3.2%(wt%) and active carbon as the positive and negative electrode, respectively, and it showed high energy densities and excellent cyclic stability.

2. Experimental

2.1 Preparation of Co_3O_4/CuO/CNTs composite

All the chemical reagents used in this study are in analytical grades without any further purification. Carbon nanotubes (outer diameter: ~80 nm, purity: ≥95%) were purchased from Shenzhen Nanotech Port Co. Ltd. Co_3O_4/CuO/CNTs composite was prepared using a hydrothermal method. Firstly, 2.91 g $Co(NO_3)_2 \cdot 6H_2O$, 0.79 g $Cu(NO_3)_2 \cdot 3H_2O$ and 3.60 g urea were dissolved in 80 mL deionized water and magnetically stirred for 30 min to form a purple solution. At the same time, the CNTs were dispersed in 20 mL deionized water and stirred for 30 min. Secondly, the above two solutions were mixed together and continuously stirred for 1 h. Thirdly, the above mixture was transferred into a 140 mL Teflon-lined autoclave and kept in an oven at 120 ºC for 6 h, and then cooled down to room temperature. After washed with deionized water and ethanol for three times, the product was dried at 80 ºC for 12 h, and then annealed at 450 ºC for 4 h to prepare for the Co_3O_4/CuO/CNTs composite.

2.2 Preparation of $CuCo_2S_4$/CNTs composite

The $CuCo_2S_4$/CNTs composites were synthesized using a sulfuration process. 0.10 g of Co_3O_4/CuO/CNTs composite was added into 30 mL of Na_2S aqueous solution (0.4 mol L^{-1}) and stirred for 10 min. Then, the above solution was kept at 80 ºC for 24 h. The obtained precipitate was washed with deionized water and ethanol for three times,

and then dried in a vacuum oven at 60 ºC for 12 h to obtain the $CuCo_2S_4$/CNTs composite. By changing the amount of CNTs (e.g., 0, 20, 50 and 80 mg) in the above preparation process of Co_3O_4/CuO/CNTs composite, the $CuCo_2S_4$, $CuCo_2S_4$/CNTs-1.3%, $CuCo_2S_4$/CNTs-3.2% and $CuCo_2S_4$/CNTs-5.0% (in wt%) were prepared, respectively.

2.3 Characterization of samples

X-ray diffraction (XRD, CuKα, 40 kV, 60 mA, Rigaku D/max-2400) was utilized to characterize the crystalline structure and average crystallite size of samples. Scanning electron microscope (SEM, InspectF50) was used to observe the morphology of samples. High-resolution transmission electron microscope (HRTEM JEM-2200FS) and selected area electron diffraction (SAED) were used for the microstructural analysis. Chemical states of elements in the composites were analyzed using X-ray photoelectron spectroscopy (XPS, KratosAxis-Ultra DLD, Japan) with a monochromatic Al Kα radiation. The specific surface area was measured by a N_2 physisorption apparatus (JW-BK122W, JWGB SCI. TECH.), and was determined using the Brunauer-Emmett-Teller (BET) theory. Fourier transform infrared (FT-IR) spectrum was obtained using an FT-IR transmittance spectrometer (Nicolet 6700, USA).

2.4 Electrochemical measurements

All the electrochemical measurements including cyclic voltammetry (CV), galvanostatic charge/discharge (GCD) and electrochemical impedance spectroscopy (EIS) were tested using an electrochemical workstation (CHI660E, Shanghai, China). To prepare a three-electrode testing set-up, the prepared slurry (80 wt% sample, 10 wt%

carbon black and 10 wt% polytetrafluoroethylene in ethanol) was coated on a piece of nickel foam (area of 1 × 1 cm^{-2}, thickness of 1 mm), which is used as the working electrode, and platinum plate and Hg/HgO were used as the counter electrode and the reference electrode, respectively. Meanwhile, a 2 M KOH aqueous solution was used as the electrolyte. CV curves were obtained at a potential window of 0~0.6 V with a scan rate ranging from 5~50 mV s^{-1}. The maximum voltage of GCDs was 0.45 V and the current density was from 1~8 A g^{-1}. The EIS test was conducted using an open circuit voltage with an amplitude of 5 mV over the frequency range of 0.01~10^5 Hz. The specific capacitances of the electrode materials were calculated from the GCD curves according to the following formula [29]:

$$C_s = \frac{I \times t}{m \times \Delta V} \quad (1)$$

where C_s is the specific capacitance (F g^{-1}), I is the discharge current (mA), t is the discharge time (s), ΔV is the potential window (V) and m is the mass of the electrode material (mg).

Asymmetric supercapacitor (ASC) devices were further assembled, in which the as-prepared nanocomposite samples were used as the positive electrode and the active carbon (AC) as the negative electrode. The mass ratio between the positive and negative materials was calculated based on the charge balance theory, according to the formula (2) [30].

$$\frac{m_+}{m_-} = \frac{C_- \times \Delta V_-}{C_+ \times \Delta V_+} \quad (2)$$

Aqueous solution of 2 M KOH and a piece of cellulose paper were used as electrolyte and separator of the ASC device, respectively.

3. Results and discussion

3.1 Material characterization

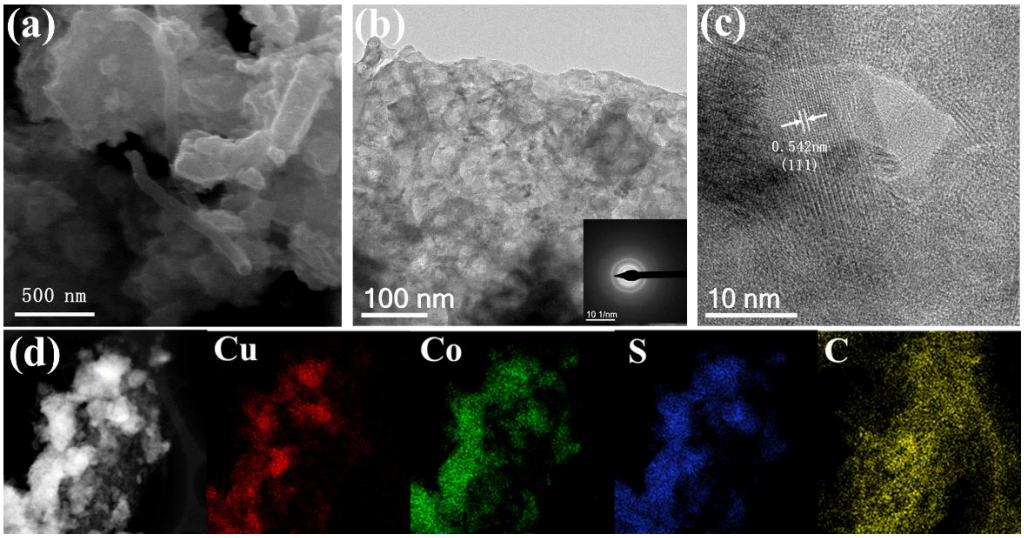

Fig. 1 (a) SEM image, (b) TEM image (the inset is the corresponding SAED pattern), (c) HR-TEM image, and (d) element mapping of the $CuCo_2S_4$/CNTs-3.2% composite.

The SEM image of $CuCo_2S_4$/CNTs-3.2% composite is shown in Fig. 1a. It can be seen that the CNTs are obviously embedded into the $CuCo_2S_4$ composite. This can provide effective paths for electron transfer and ion diffusion in the energy storage processes, and thus is favorable for the faradaic redox reactions on the surface of the $CuCo_2S_4$/CNTs composite. Fig. 1b shows a TEM image of $CuCo_2S_4$/CNTs. Clearly, there are many nano-pores in the composite, which can significantly increase the contact areas between electrode materials and electrolyte. The selected area electron diffraction (SAED) in Fig. 1b shows the polycrystalline nature of $CuCo_2S_4$. The lattice fringe shown in Fig. 1c is about 0.542 nm, which can be indexed to the (111) crystal plane of the $CuCo_2S_4$. Furthermore, the EDX mappings shown in Fig. 1d demonstrate

that elements of Cu, Co, S and C are uniformly distributed within the $CuCo_2S_4$/CNTs-3.2% composite.

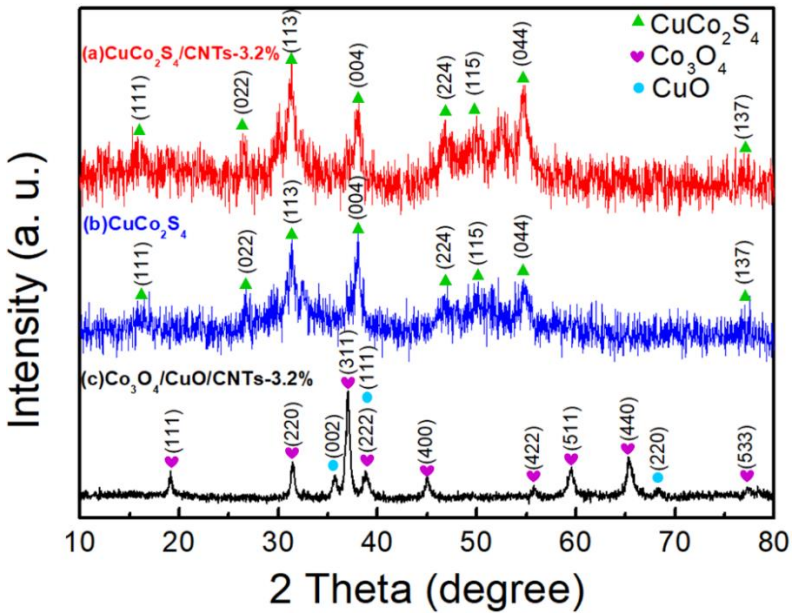

Fig. 2 XRD spectra of (a) $CuCo_2S_4$/CNTs-3.2%, (b) $CuCo_2S_4$ and (c) Co_3O_4/CuO/CNTs-3.2%.

XRD spectra of Co_3O_4/CuO/CNTs-3.2%, $CuCo_2S_4$ and $CuCo_2S_4$/CNTs-3.2% are shown in Fig. 2. From the XRD spectrum of the sample before sulfuration process shown in Fig. 2c, it is found that some diffraction peaks are corresponding to (111), (220), (311), (222), (400), (422), (511), (440) and (533) of the Co_3O_4 phase (JCPDS card No. 42-1467), while the left diffraction peaks are corresponding to (002), (111) and (220) of the CuO phase (JCPDS card No. 44-0706). This indicates that the sample obtained after the hydrothermal and post-annealing process is a mixture of Co_3O_4 and CuO crystals.

Figs. 2a and 2b present the XRD spectra of the samples with and without CNTs after the sulfuration process, respectively. All the diffraction peaks are well indexed to (022), (113), (004), (224), (115) and (044) of the $CuCo_2S_4$ phase (JCPDS card No. 42-1450).

Therefore, it reveals that the Co_3O_4 and CuO crystals have been completely transformed into the $CuCo_2S_4$ crystals after the sulfuration process based on the following equation:

$$2Co_3O_4 + 3CuO + 12Na_2S + 13H_2O \rightarrow 3CuCo_2S_4 + 24NaOH + H_2 \quad (3)$$

Due to the low amount of CNTs, their XRD diffraction peaks cannot be detected. Furthermore, the crystal sizes (L) of $CuCo_2S_4$ and $CuCo_2S_4$/CNTs-3.2% composite were calculated using the Scherrer formula (4):

$$L = \frac{K\lambda}{\beta\cos\theta} \quad (4)$$

where K is a constant (0.89), λ is the X-ray wavelength (0.15406 nm), β is the line width of peak at half maximum height and θ is the diffracting angle. The average crystal sizes of $CuCo_2S_4$ for the pure $CuCo_2S_4$ and $CuCo_2S_4$/CNTs-3.2% composite were calculated to be 24.9 and 12.8 nm, respectively. Addition of CNTs reduces the average crystal sizes of $CuCo_2S_4$, which is probably because the presence of CNTs could separate and restrict the aggregation of $CuCo_2S_4$ nanocrystals, and thus inhibit their growth [31]. Moreover, the specific surface area of $CuCo_2S_4$/CNTs-3.2% is 14.1 m^2g^{-1}, which is larger than that of $CuCo_2S_4$ (e.g., 8.9 m^2g^{-1}). Therefore, the $CuCo_2S_4$/CNTs-3.2% composite shows much smaller crystal size and larger specific surface area than those of the pristine $CuCo_2S_4$, which are beneficial for the redox reactions in the energy storage processes of supercapacitors.

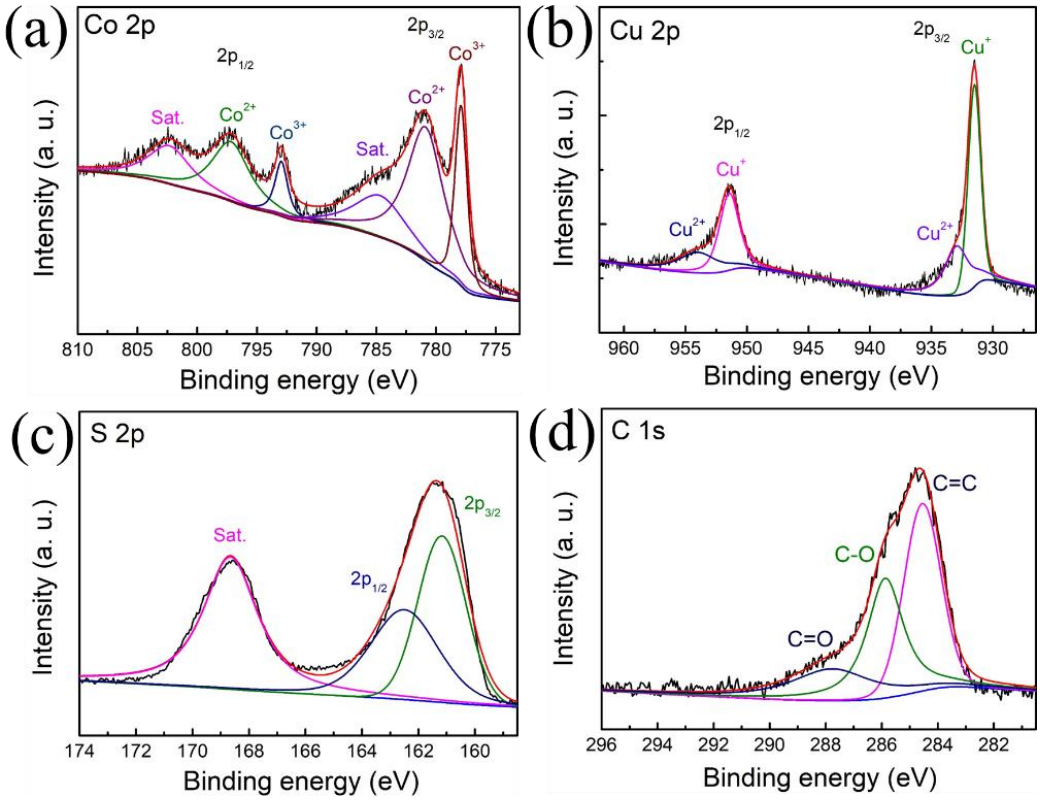

Fig. 3 XPS spectra of (a) Co 2p, (b) Cu 2p, (c) S 2p and (d) C 1s of $CuCo_2S_4$/CNTs-3.2%

Fig. 3 shows XPS spectra of Co 2p, Cu 2p, S 2p and C 1s of the $CuCo_2S_4$/CNTs-3.2% composite. The peaks at 797.2 and 781.0 eV in Fig. 3a are corresponding to Co^{3+}, and the peaks at 792.9 and 777.8 eV are corresponding to Co^{2+} [32, 33]. The Cu 2p spectrum can be deconvoluted into two spin-orbit doublets as shown in Fig. 3b. The peaks at 954.1 and 933.0 eV of the Cu 2p spectra can be assigned to Cu^{2+}, whereas the peaks at 951.4 and 931.5 eV can be assigned to Cu^{+} [34]. For the S 2p spectrum shown in Fig. 3c, there are two major peaks at 162.5 and 161.2 eV, which can be indexed to S $2p_{1/2}$ and S $2p_{3/2}$, respectively [28, 35]. Moreover, the C 1s spectrum shown in Fig. 3d can be fitted by three peaks at 284.5, 285.8 and 287.8 eV, which are attributed to C=C group in the CNTs, C-O and C=O groups on the surfaces of CNTs, respectively [36].

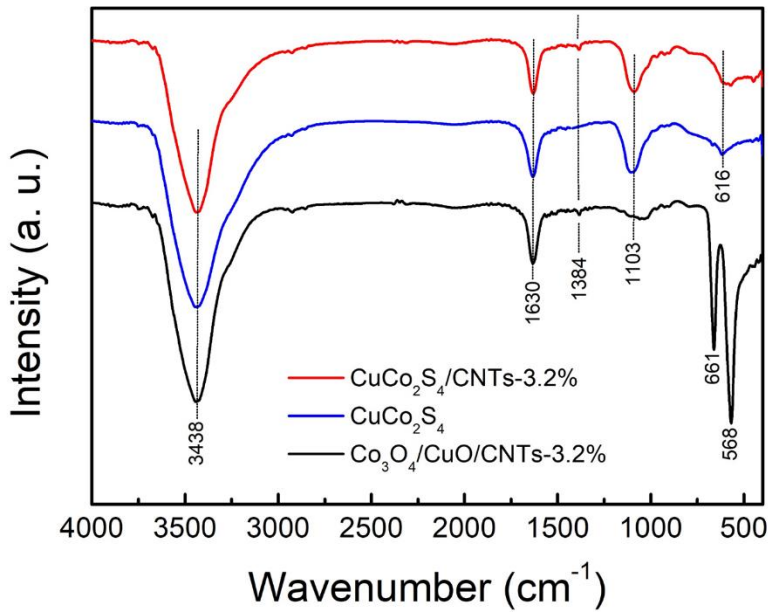

Fig. 4 FT-IR spectra of $CuCo_2S_4$/CNTs-3.2%, $CuCo_2S_4$ and Co_3O_4/CuO/CNTs-3.2%.

Fig. 4 shows the FT-IR spectra of $CuCo_2S_4$, $CuCo_2S_4$/CNTs-3.2% and Co_3O_4/CuO/CNTs-3.2%. The vibration peaks related to O-H bonding at 3438 and 1630 cm^{-1} are observed in all spectra of $CuCo_2S_4$, $CuCo_2S_4$/CNTs-3.2% and Co_3O_4/CuO/CNTs-3.2%, indicating that there are many hydroxyl groups on their surfaces. The peak at 1384 cm^{-1} in the spectra of $CuCo_2S_4$/CNTs-3.2% and Co_3O_4/CuO/CNTs-3.2% is attributed to the stretching vibration C−OH mode from the CNTs [37]. The Co-S and Cu-S stretching modes are observed at 1103 cm^{-1} and 616 cm^{-1} in the spectra of $CuCo_2S_4$ and $CuCo_2S_4$/CNTs-3.2% [38, 39]. The peaks at 661 and 568 cm^{-1} in the spectrum of Co_3O_4/CuO/CNTs-3.2% are attributed to the Co-O stretching vibration mode [40]. The peak at 661 cm^{-1} is assigned to tetrahedrally co-ordinated Co(II)-O, and the peak at 568 cm^{-1} is assigned to octahedrally co-ordinated Co(III)-O, which confirm the formation of Co_3O_4 in the precursor [41]. Because of the intensity overlapping of the vibration peaks, the peak at 568 cm^{-1} in the spectrum of

Co_3O_4/CuO/CNTs-3.2% is also contributed by the Cu-O stretching vibration mode [42].

3.2 Electrochemical characterization

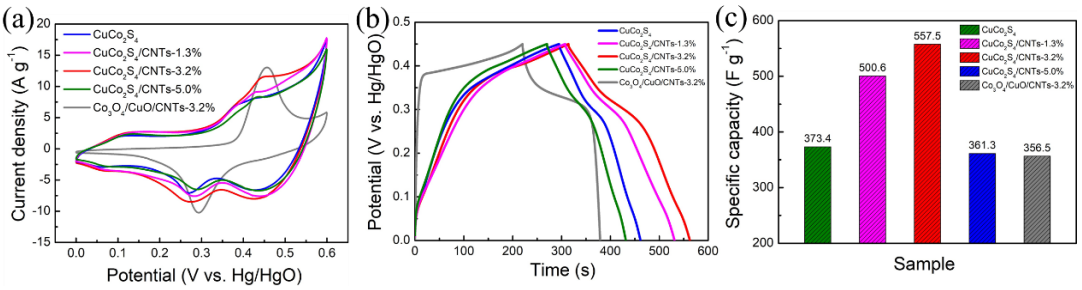

Fig. 5 (a) CV curves of $CuCo_2S_4$, $CuCo_2S_4$/CNTs-1.3%, 3.2%, 5.0% and Co_3O_4/CuO/CNTs-3.2% at 10 mV s^{-1}, (b) GCD curves of $CuCo_2S_4$, $CuCo_2S_4$/CNTs-1.3%, 3.2%, 5.0% and Co_3O_4/CuO/CNTs-3.2% at 1 A g^{-1}, (c) specific capacitances of $CuCo_2S_4$, $CuCo_2S_4$/CNTs-1.3%, 3.2%, 5.0% and Co_3O_4/CuO/CNTs-3.2% at 1 A g^{-1}.

Electrochemical performance of the pristine $CuCo_2S_4$, $CuCo_2S_4$/CNTs and Co_3O_4/CuO/CNTs electrodes was investigated using a three-electrode system in a 2 M KOH aqueous electrolyte. Fig. 5a shows the CV curves of $CuCo_2S_4$, $CuCo_2S_4$/CNTs-1.3%, 3.2%, 5.0% and Co_3O_4/CuO/CNTs-3.2% at a scan rate of 10 mV s^{-1} in the potential range of 0~0.6 V. It can be seen that all the CV curves show closed patterns and have a pair of redox peaks, indicating that the energy storage mechanism of these electrodes is based on the Faradaic redox reaction processes as shown in the following equations [43-46]:

$$CuCo_2S_4 + OH^- + H_2O \leftrightarrow CuSOH + 2CoSOH + e^- \quad (5)$$

$$CoSOH + OH^- \leftrightarrow CoSO + H_2O + e^- \quad (6)$$

$$CuSOH + OH^- \leftrightarrow CuSO + H_2O + e^- \quad (7)$$

$$Co_3O_4 + OH^- + H_2O \leftrightarrow 3CoOOH + e^- \quad (8)$$

$$CoOOH + OH^- \leftrightarrow CoO_2 + H_2O + e^- \quad (9)$$

$$2CuO + H_2O + 2e^- \leftrightarrow Cu_2O + 2OH^- \quad (10)$$

It is clear that the CV integrated area of the $CuCo_2S_4$/CNTs-3.2% electrode is much larger than those of the other electrodes, e.g., $CuCo_2S_4$, $CuCo_2S_4$/CNTs-1.3% and $CuCo_2S_4$/CNTs-5 .0%, demonstrating that the $CuCo_2S_4$/CNTs-3.2% electrode has the highest capacitance under the same scan rate. The longest discharge time of the $CuCo_2S_4$/CNTs-3.2% electrode among those of all other electrodes as shown in Fig. 5b further exhibits its highest capacitance. The specific capacitances were calculated from the data of the GCD curves in Fig. 5c using the formula (1). The specific capacitance is increased from 373.4 to 557.5 F g^{-1} with the increase of CNTs contents from 0 to 3.2%. However, when the content of CNTs is further increased to 5.0%, the specific capacitance is decreased. Therefore, the optimum CNTs content in the $CuCo_2S_4$/CNTs composites is about 3.2%. Adding the appropriate amount of CNTs increases the effective paths for electron transfer and electrolyte ion diffusion, and also increases the specific contact surface areas between electrolyte ions and $CuCo_2S_4$ electrode material, all of which facilitate the faradaic redox reactions on the surface of $CuCo_2S_4$. However, because of the low capacitance of CNTs, excess CNTs will result in the reduction of the capacitance of Co_3O_4/CuO/CNTs composite. Therefore, the specific capacitance of the $CuCo_2S_4$/CNTs-5.0% composite is thus decreased. Moreover, the CV integrated area and the discharge time of the $CuCo_2S_4$/CNTs-3.2% electrode are much larger than those of the Co_3O_4/CuO/CNTs-3.2% electrode, clearly indicating that the specific capacitance

of the $CuCo_2S_4$/CNTs-3.2% electrode is higher than that of the Co_3O_4/CuO/CNTs-3.2% (356.5 F g^{-1}). The improvement in the capacitance is mainly attributed to the more active sites and lower resistance of $CuCo_2S_4$/CNTs-3.2% than those of the metal oxides [20].

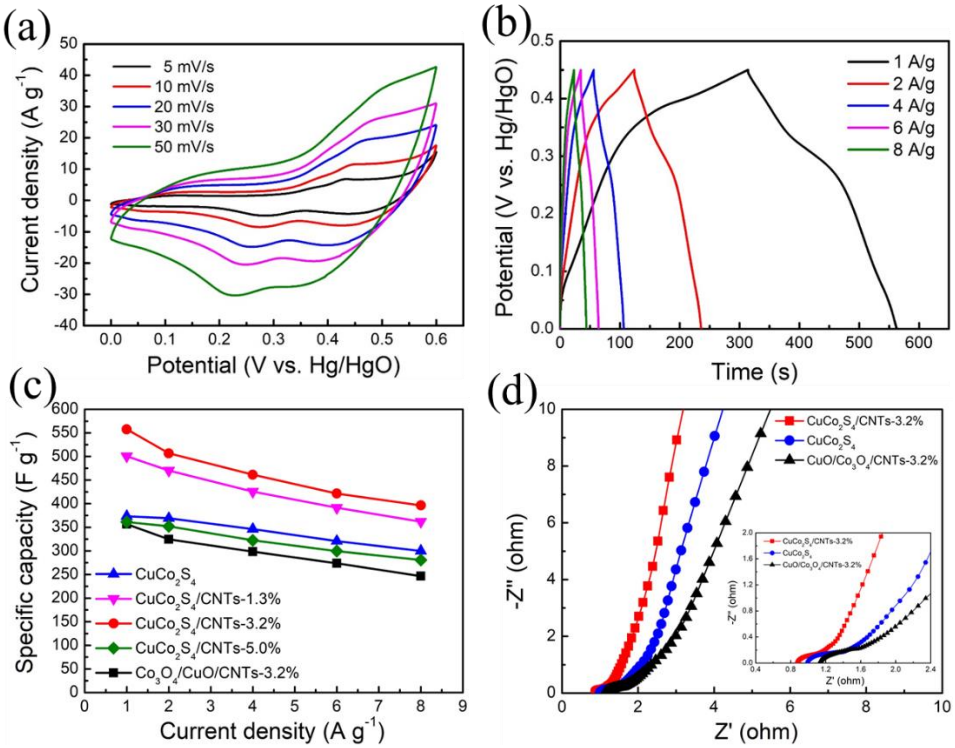

Fig. 6 (a)CV curves of $CuCo_2S_4$/CNTs-3.2% at different scan rates, (b) GCD curves of $CuCo_2S_4$/CNTs-3.2% at different current densities, (c) specific capacitance readings of $CuCo_2S_4$, $CuCo_2S_4$/CNTs-1.3%, 3.2% and 5.0% and (d) Nyquist plots of $CuCo_2S_4$, $CuCo_2S_4$/CNTs-3.2% and Co_3O_4/CuO/CNTs-3.2% (the inset is the expanded high-frequency region of the plots).

Table 1 The specific capacitance, series resistance and charge transfer resistance of all samples.

Samples	C_s (F g^{-1}) at 1 A g^{-1}	R_s (Ω)	R_{ct} (Ω)
$CuCo_2S_4$	373.4	0.99	0.62
$CuCo_2S_4$/CNTs-1.3%	500.6	0.91	0.47
$CuCo_2S_4$/CNTs-3.2%	557.5	0.87	0.40
$CuCo_2S_4$/CNTs-5.0%	361.3	0.84	0.38
Co_3O_4/CuO/CNTs-3.2%	356.5	1.13	0.92

Fig. 6a shows the CV curves of the $CuCo_2S_4$/CNTs-3.2% electrode at different scan rates ranging from 5~50 mV s^{-1}. Because of the polarization effect of the electrode material, the positions of the oxidation/reduction peaks slightly move towards positive/negative potentials, respectively, with the increase of scan rate.[47, 48]. The obtained GCD curves of the $CuCo_2S_4$/CNTs-3.2% electrode at different current densities are shown in Fig. 6b. It can be seen that all the curves are nonlinear, indicating its pseudo-capacitance nature based on Faraday redox reactions. The specific capacitance values of the $CuCo_2S_4$/CNTs-3.2% electrode are 557.5, 506.7, 461.3, 421.4 and 396.4 F g^{-1} at current densities of 1, 2, 4, 6 and 8 A g^{-1}, respectively. These values are much higher than those of the other electrodes tested at different current densities as shown in Fig. 6c.

The EIS measurement was further carried out to investigate the electrochemical kinetics of $CuCo_2S_4$, $CuCo_2S_4$/CNTs-3.2% and Co_3O_4/CuO/CNTs-3.2% electrodes. The obtained Nyquist plots are presented in Fig. 6d. All the curves display similar Nyquist plots, which consist of a semicircle in the high frequency region and a straight

line in the low frequency region. The intercept at the real axis in the high frequency region represents the series resistance (R_s), which includes the intrinsic resistance of the electrode materials/electrolyte and the contact resistance between electrode materials and current collector [49]. The diameter of the semicircle in the high frequency region is related to the charge-transfer resistance (R_{ct}), and the slope of the inclined line in the lower frequency region represents the Warburg impedance (W), which is attributed to the ion diffusion in the electrolyte at the electrode interface [50, 51]. The obtained R_s and R_{ct} values of the $CuCo_2S_4$/CNTs-3.2% electrode are 0.87Ω and 0.40 Ω, respectively, which are much smaller than those of the pristine $CuCo_2S_4$ electrode (0.99Ω and 0.62 Ω) and the Co_3O_4/CuO/CNTs-3.2% electrode (1.13Ω and 0.92Ω), all of which are listed in Table 1. Therefore, the $CuCo_2S_4$/CNTs-3.2% electrode has lower series resistance and charge transfer resistance. In addition, the larger slope of the inclined line for the $CuCo_2S_4$/CNTs-3.2% electrode means that it has a much lower ion diffusion resistance than those of other electrodes. These results mean that the CNTs in $CuCo_2S_4$ composite can provide effective paths for both electron transfer and ion diffusion, which is favorable for faradaic redox reactions in energy storage processes, as schematically illustrated in Fig. 7.

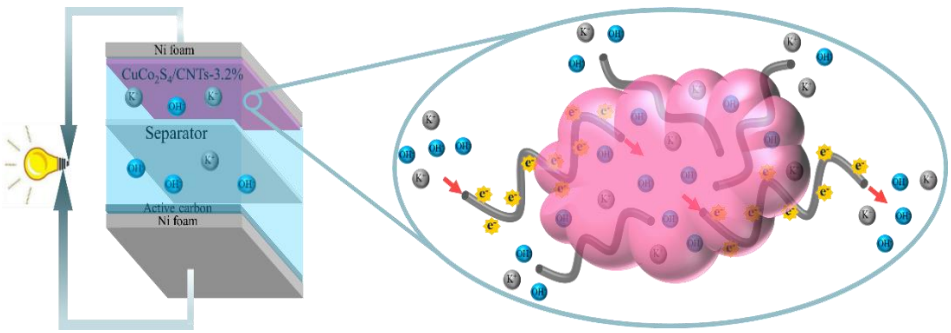

Fig. 7 Schematic illustration of $CuCo_2S_4$/CNTs-3.2%//AC device and the electron transfer

and ion diffusion of $CuCo_2S_4$/CNTs composite.

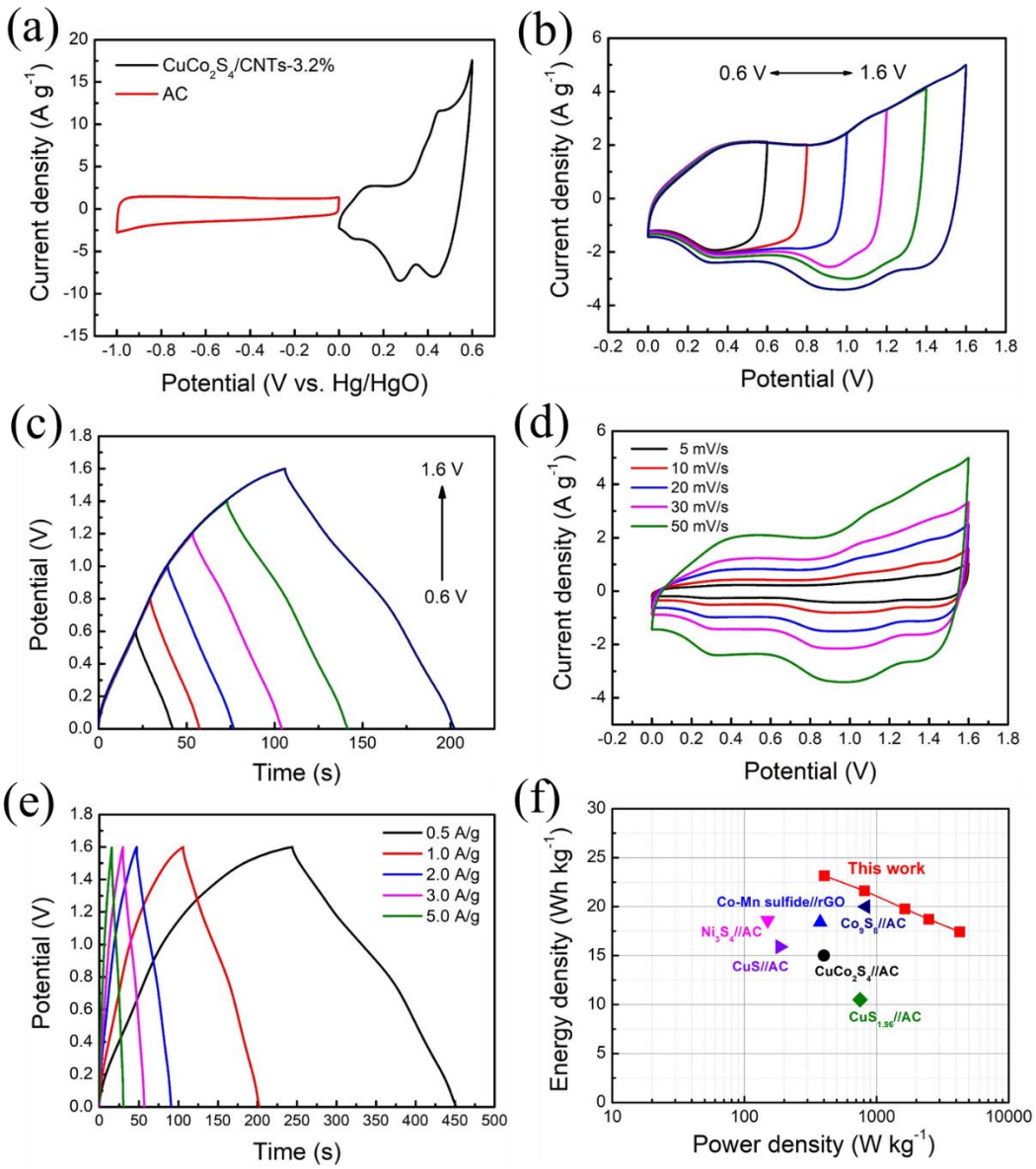

Fig. 8 (a) CV curves of $CuCo_2S_4$/CNTs-3.2% and AC electrodes at a scan rate of 10 mV s^{-1}, (b) CV curves of the device at a scan rate of 50 mV s^{-1} in different potential windows, (c) GCD curves of the device at a current density of 1 A g^{-1} in different potential windows, (d) CV curves of the device at different scan rates, (e) GCD curves of the device at different current densities, (f) Ragone plot of the device.

To further investigate the practical application of the $CuCo_2S_4$/CNTs-3.2% composite, an ASC device was tested, using $CuCo_2S_4$/CNTs-3.2% and active carbon (AC) as the positive and negative electrodes respectively (see Fig. 7). The operating potential window of the ASC device was obtained by measuring the CV curves of the positive and negative electrodes separately using the three-electrode system as shown in Fig. 8a. The obtained potential windows of positive and negative electrodes are 0~0.6 V and -1~0 V, respectively. Therefore, the appropriate potential window of the ASC device is about 1.6 V.

In addition, the CV and GCD curves of the ASC device measured in the high potential range from 0.6~1.6 V are shown in Figs. 8b and 8c. At the highest voltage of 1.6 V in CV curves, no obvious oxygen evolution reaction observed, indicating that the maximum voltage can be increased up to 1.6 V [52]. The GCD curves show that the ASC device can work stably at the highest voltage of 1.6 V. Fig. 8d shows the CV curves of the ASC device tested at different scan rates. A pair of obvious redox peaks appear in all the CV curves, indicating the redox characteristic of $CuCo_2S_4$/CNTs-3.2% composite generated from the Faradaic reaction process. Based on Fig. 8e (the GCD curves of the device obtained at different scan rates), the specific capacitance (C_d) of the device can be calculated using the following formula (11), and the results are 65.1, 60.8, 55.6, 52.6 and 49.0 F g^{-1} at different current densities 0.5, 1, 2, 3 and 5 A g^{-1}, respectively.

$$C_d = \frac{I \times t}{M \times \Delta V} \tag{11}$$

where M (mg) is the total mass of the positive and negative electrodes. The energy

density and power density of the ASC device can be calculated using formula (12) and (13) [53-55].

$$E = \frac{C_d \times \Delta V^2}{2 \times 3.6} \quad (12)$$

$$P = \frac{E \times 3600}{\Delta t} \quad (13)$$

Based on these density values, the Ragone plots of the ASC device can be obtained and the results are shown in Fig. 8f. Notably, the ASC device displays a high energy density of 23.2 Wh kg^{-1} at a power density of 402.7 W kg^{-1}. Even at a high power density of 4266.7 W kg^{-1}, the device still has an energy density of 17.4 Wh kg^{-1}. The obtained energy and power density of the $CuCo_2S_4$/CNTs-3.2%//AC device are much better than those of metal sulfide based ASC devices reported in literature (see Fig. 8(f)), such as $CuCo_2S_4$//AC (15 Wh kg^{-1} at 400 W kg^{-1}) [56], Co-Mn sulfide//rGO (18.4 Wh kg^{-1} at 375 W kg^{-1}) [57], Ni_3S_4//AC (18.6 Wh kg^{-1} at 150 W kg^{-1}) [58], $CuS_{1.96}$//AC (10.5 Wh kg^{-1}at 750 W kg^{-1}) [59], Co_9S_8//AC (20.0 Wh kg^{-1} at 828.5 W kg^{-1}) [60] and CuS//AC (15.9 Wh kg^{-1} at 185.4 W kg^{-1}) [49].

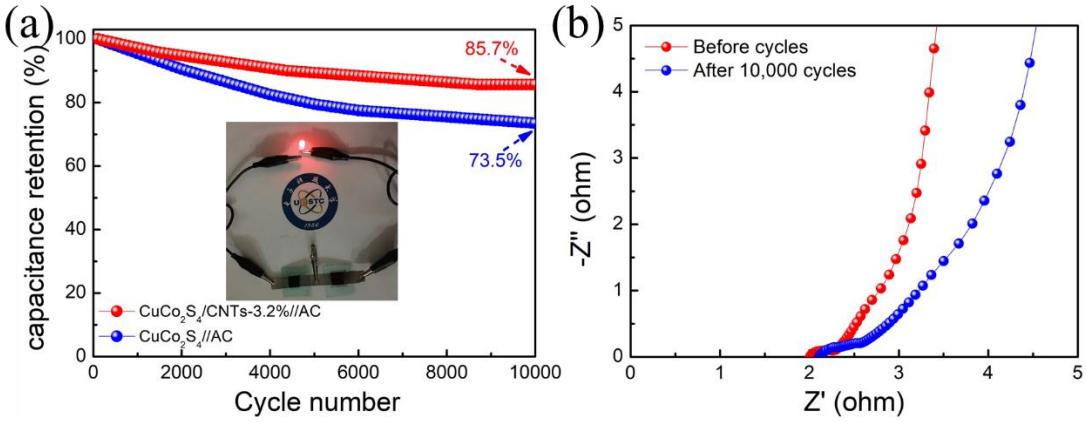

Fig. 9 (a) Cycling stability of the $CuCo_2S_4$/CNTs-3.2%//AC and $CuCo_2S_4$//AC device (insert photograph of lighting LED bulb), (b) Nyquist plot of the $CuCo_2S_4$/CNTs-3.2%//AC device before and after 10000 cycles.

The cyclic stability is one of the critical factors for the successful application of supercapacitors. The cyclic stabilities of the $CuCo_2S_4$//AC and $CuCo_2S_4$/CNTs-3.2%//AC devices were tested at a current density of 3 A g^{-1} and the obtained capacitances values after 10000 cycles are shown in Fig. 9a. The capacitance of the $CuCo_2S_4$/CNTs-3.2%//AC device is 45.1 F g^{-1} after 10000 cycles, which retains 85.7% of its initial value. This value is much higher than that of the $CuCo_2S_4$//AC device (e.g., 73.5%). It is also higher than those of previous reported $CuCo_2S_4$ based ASC devices in literature [61-63], indicating the excellent cyclic stability of the $CuCo_2S_4$/CNTs-3.2%//AC device due to the addition of CNTs. Fig. 9b shows the EIS curves of the $CuCo_2S_4$/CNTs-3.2%//AC device before and after testing for 10000 cycles. The values of R_s (2.12 Ω) and R_{ct} (0.67 Ω) are all quite small after 10,000 cycles, indicating that the $CuCo_2S_4$/CNTs-3.2% composite still maintains a good performance after long-term and repeated charges/discharges. Therefore, the $CuCo_2S_4$/CNTs-3.2% composite can be used as a good electrode material for supercapacitors with excellent electrochemical performance.

4. Conclusion

In summary, the $CuCo_2S_4$/CNTs composites have successfully been prepared using hydrothermal and sulfuration process. Appropriate amount of CNTs in the $CuCo_2S_4$ composite can increase the specific surface areas, reduce the series and charge transfer resistances and enhance cycle stability during long-term charges and discharges. When the content of CNTs is 3.2% in the composite, the specific capacitance of

$CuCo_2S_4$/CNTs composite is increased up to 557.5 F g^{-1} from 373.4 F g^{-1} of the pristine $CuCo_2S_4$ at 1 A g^{-1}. In addition, the specific capacitance of the Co_3O_4/CuO/CNTs- 3.2% composite is only 356.5 F g^{-1} at 1 A g^{-1}, which is much lower than that of the $CuCo_2S_4$/CNTs-3.2% composite. The $CuCo_2S_4$/CNTs-3.2%//AC ASC device shows a good energy density of 23.2 Wh kg^{-1} at a power density of 402.7 W kg^{-1}, and exhibits a better cycle stability than those previous reported $CuCo_2S_4$ based ASC devices, even after 10000 cycles. Therefore, adding the CNTs into the binary metal sulfides is an attractive strategy for the development of high-performance energy storage systems.

Acknowledgements

Funding supports from UK Engineering Physics and Science Research Council (EPSRC EP/P018998/1), Newton Mobility Grant (IE161019) through Royal Society and NFSC, and Royal academy of Engineering UK-Research Exchange with China and India are acknowledged.

Reference

[1] X. Liu, J. Liu, X. Sun, NiCo2O4@NiO hybrid arrays with improved electrochemical performance for pseudocapacitors, J. Mater. Chem. A, 3 (2015) 13900-13905.
[2] G. Liu, B. Wang, L. Wang, T. Liu, T. Gao, D. Wang, Facile controlled synthesis of a hierarchical porous nanocoral-like Co3S4 electrode for high-performance supercapacitors, RSC Adv., 6 (2016) 54076-54086.
[3] J. Zhao, Z. Li, X. Yuan, T. Shen, L. Lin, M. Zhang, A. Meng, Q. Li, Novel core-shell multi-dimensional hybrid nanoarchitectures consisting of Co(OH)2 nanoparticles/Ni3S2 nanosheets grown on SiC nanowire networks for high-performance asymmetric supercapacitors, Chem. Eng. J., 357 (2019) 21-32.
[4] S. Hussain, E. Kovacevic, R. Amade, J. Berndt, C. Pattyn, A. Dias, C. Boulmer-Leborgne, M.-R. Ammar, E. Bertran-Serra, Plasma synthesis of polyaniline enrobed carbon nanotubes for electrochemical applications, Electrochim. Acta, 268 (2018) 218-225.
[5] H.-Y. Wang, D.-G. Li, H.-L. Zhu, Y.-X. Qi, H. Li, N. Lun, Y.-J. Bai, Mn 3 O 4 /Ni(OH) 2 nanocomposite as an applicable electrode material for pseudocapacitors, Electrochim. Acta, 249 (2017) 155-165.
[6] S. Ghasemi, M. Jafari, F. Ahmadi, Cu 2 O-Cu(OH) 2 -graphene nanohybrid as new capacitive

material for high performance supercapacitor, Electrochim. Acta, 210 (2016) 225-235.
[7] G.-C. Li, M. Liu, M.-K. Wu, P.-F. Liu, Z. Zhou, S.-R. Zhu, R. Liu, L. Han, MOF-derived self-sacrificing route to hollow NiS2/ZnS nanospheres for high performance supercapacitors, RSC Adv., 6 (2016) 103517-103522.
[8] S. Sun, L. Guo, X. Chang, Y. Yu, X. Zhai, MnO2/g-C3N4@PPy nanocomposite for high-performance supercapacitor, Mater. Lett., 236 (2019) 558-561.
[9] R. Ravit, J. Abdullah, I. Ahmad, Y. Sulaiman, Electrochemical performance of poly(3, 4-ethylenedioxythipohene)/nanocrystalline cellulose (PEDOT/NCC) film for supercapacitor, Carbohydr Polym, 203 (2019) 128-138.
[10] J. Zhang, H. Guan, Y. Liu, Y. Zhao, B. Zhang, Hierarchical polypyrrole nanotubes@NiCo 2 S 4 nanosheets core-shell composites with improved electrochemical performance as supercapacitors, Electrochim. Acta, 258 (2017) 182-191.
[11] A. Mohammadi, N. Arsalani, A.G. Tabrizi, S.E. Moosavifard, Z. Naqshbandi, L.S. Ghadimi, Engineering rGO-CNT wrapped Co 3 S 4 nanocomposites for high-performance asymmetric supercapacitors, Chem. Eng. J., 334 (2018) 66-80.
[12] B. Xin, Y. Zhao, C. Xu, A high mass loading electrode based on ultrathin Co3S4 nanosheets for high performance supercapacitor, J. Solid State Electr., 20 (2016) 2197-2205.
[13] J.S. Chen, Y. Gui, D.J. Blackwood, Self-supported phase-pure Ni 3 S 2 sheet-on-rod nanoarrays with enhanced pseudocapacitive properties and high energy density, J. Power Sources, 325 (2016) 575-583.
[14] Y.-P. Gao, K.-J. Huang, X. Wu, Z.-Q. Hou, Y.-Y. Liu, MoS 2 nanosheets assembling three-dimensional nanospheres for enhanced-performance supercapacitor, J. Alloy. Compd., 741 (2018) 174-181.
[15] R.K. Mishra, M. Krishnaih, S.Y. Kim, A.K. Kushwaha, S.H. Jin, Binder-free, scalable hierarchical MoS2 as electrode materials in symmetric supercapacitors for energy harvesting applications, Mater. Lett., 236 (2019) 167-170.
[16] C. Justin Raj, B.C. Kim, W.-J. Cho, W.-G. Lee, Y. Seo, K.-H. Yu, Electrochemical capacitor behavior of copper sulfide (CuS) nanoplatelets, J. Alloy. Compd., 586 (2014) 191-196.
[17] X. Li, K. Zhou, J. Zhou, J. Shen, M. Ye, CuS nanoplatelets arrays grown on graphene nanosheets as advanced electrode materials for supercapacitor applications, Journal of Materials Science & Technology, 34 (2018) 2342-2349.
[18] C. Wei, N. Zhan, J. Tao, S. Pang, L. Zhang, C. Cheng, D. Zhang, Synthesis of hierarchically porous NiCo 2 S 4 core-shell hollow spheres via self-template route for high performance supercapacitors, Appl. Surf. Sci., 453 (2018) 288-296.
[19] A. Pramanik, S. Maiti, T. Dhawa, M. Sreemany, S. Mahanty, High faradaic charge storage in ZnCo2S4 film on Ni-foam with a hetero-dimensional microstructure for hybrid supercapacitor, Materials Today Energy, 9 (2018) 416-427.
[20] W. Xu, J. Lu, W. Huo, J. Li, X. Wang, C. Zhang, X. Gu, C. Hu, Direct growth of CuCo2S4 nanosheets on carbon fiber textile with enhanced electrochemical pseudocapacitive properties and electrocatalytic properties towards glucose oxidation, Nanoscale, 10 (2018) 14304-14313.
[21] A.M. Elshahawy, X. Li, H. Zhang, Y. Hu, K.H. Ho, C. Guan, J. Wang, Controllable MnCo2S4 nanostructures for high performance hybrid supercapacitors, J. Mater. Chem. A, 5 (2017) 7494-7506.
[22] H. Tong, W. Bai, S. Yue, Z. Gao, L. Lu, L. Shen, S. Dong, J. Zhu, J. He, X. Zhang, Zinc cobalt

sulfide nanosheets grown on nitrogen-doped graphene/carbon nanotube film as a high-performance electrode for supercapacitors, J. Mater. Chem. A, 4 (2016) 11256-11263.
[23] Y. Huang, Y. Zhao, J. Bao, J. Lian, M. Cheng, H. Li, Lawn-like FeCo2S4 hollow nanoneedle arrays on flexible carbon nanofiber film as binder-free electrodes for high-performance asymmetric pseudocapacitors, J. Alloy. Compd., 772 (2019) 337-347.
[24] P. Sun, R. Wang, Q. Wang, H. Wang, X. Wang, Uniform MoS2 nanolayer with sulfur vacancy on carbon nanotube networks as binder-free electrodes for asymmetrical supercapacitor, Appl. Surf. Sci., 475 (2019) 793-802.
[25] L. Chen, Y. Zuo, Y. Zhang, Y. Gao, A novel CuCo 2 S 4 /polyacrylonitrile ink for flexible film supercapacitors, Mater. Lett., 215 (2018) 268-271.
[26] M. Yu, Y. Han, Y. Li, J. Li, L. Wang, Improving electrochemical activity of activated carbon derived from popcorn by NiCo2S4 nanoparticle coating, Appl. Surf. Sci., 463 (2019) 1001-1010.
[27] M.A.A. Mohd Abdah, N.S. Mohd Razali, P.T. Lim, S. Kulandaivalu, Y. Sulaiman, One-step potentiostatic electrodeposition of polypyrrole/graphene oxide/multi-walled carbon nanotubes ternary nanocomposite for supercapacitor, Mater. Chem. Phys., 219 (2018) 120-128.
[28] R. Jin, Y. Cui, S. Gao, S. Zhang, L. Yang, G. Li, CNTs@NC@CuCo 2 S 4 nanocomposites: An advanced electrode for high performance lithium-ion batteries and supercapacitors, Electrochim. Acta, 273 (2018) 43-52.
[29] X. Ma, Z. Kang, A facile electrodeposition technique for synthesis of nickel sulfides/carbon nanotubes nanocomposites as high performance electrodes for supercapacitor, Mater. Lett., 236 (2019) 468-471.
[30] G. Saeed, S. Kumar, N.H. Kim, J.H. Lee, Fabrication of 3D graphene-CNTs/α-MoO3 hybrid film as an advance electrode material for asymmetric supercapacitor with excellent energy density and cycling life, Chem. Eng. J., 352 (2018) 268-276.
[31] H. Kwon, G.-G. Lee, S.-G. Kim, B.-W. Lee, W.-C. Seo, M. Leparoux, Mechanical properties of nanodiamond and multi-walled carbon nanotubes dual-reinforced aluminum matrix composite materials, Materials Science and Engineering: A, 632 (2015) 72-77.
[32] S. Cheng, T. Shi, C. Chen, Y. Zhong, Y. Huang, X. Tao, J. Li, G. Liao, Z. Tang, Construction of porous CuCo2S4 nanorod arrays via anion exchange for high-performance asymmetric supercapacitor, Sci Rep, 7 (2017) 6681.
[33] P. Xia, Q. Wang, Y. Wang, W. Quan, D. Jiang, M. Chen, Hierarchical NiCo2O4@Ni(OH)2 core-shell nanoarrays as advanced electrodes for asymmetric supercapacitors with high energy density, J. Alloy. Compd., 771 (2019) 784-792.
[34] L. Chen, Facile Synthesis of Ultrathin CuCo2S4 Nanosheets for High- Performance Supercapacitors, International Journal of Electrochemical Science, (2018) 1343-1354.
[35] X. Li, J. Sun, L. Feng, L. Zhao, L. Ye, W. Zhang, L. Duan, Cactus-like ZnS/Ni 3 S 2 hybrid with high electrochemical performance for supercapacitors, J. Alloy. Compd., 753 (2018) 508-516.
[36] Y. Zou, C. Cai, C. Xiang, P. Huang, H. Chu, Z. She, F. Xu, L. Sun, H.-B. Kraatz, Simple synthesis of core-shell structure of Co–Co 3 O 4 @ carbon-nanotube-incorporated nitrogen-doped carbon for high-performance supercapacitor, Electrochim. Acta, 261 (2018) 537-547.
[37] B.S. Singu, K.R. Yoon, Highly exfoliated GO-PPy-Ag ternary nanocomposite for electrochemical supercapacitor, Electrochim. Acta, 268 (2018) 304-315.
[38] S. Vadivel, B. Paul, A. Habibi-Yangjeh, D. Maruthamani, M. Kumaravel, T. Maiyalagan, One-pot hydrothermal synthesis of CuCo2S4/RGO nanocomposites for visible-light photocatalytic

applications, Journal of Physics and Chemistry of Solids, 123 (2018) 242-253.
[39] M.M. Mezgebe, A. Ju, G. Wei, D.K. Macharia, S. Guang, H. Xu, Structure based optical properties and catalytic activities of hydrothermally prepared CuS nanostructures, Nanotechnology, 30 (2019) 105704.
[40] N. Liu, P. Tao, C. Jing, W. Huang, X. Zhang, M. Wu, J. Lei, L. Tang, A facile fabrication of nanoflower-like Co3O4 catalysts derived from ZIF-67 and their catalytic performance for CO oxidation, J. Mater. Sci., 53 (2018) 15051-15063.
[41] M. Roy, S. Ghosh, M.K. Naskar, Synthesis of morphology controllable porous Co3O4 nanostructures with tunable textural properties and their catalytic application, Dalton T., 43 (2014) 10248-10257.
[42] M. Fang, R. Zheng, Y. Wu, D. Yue, X. Qian, Y. Zhao, Z. Bian, CuO nanosheet as a recyclable Fenton-like catalyst prepared from simulated Cu(ii) waste effluents by alkaline H2O2 reaction, Environmental Science: Nano, 6 (2019) 105-114.
[43] H. You, L. Zhang, Y. Jiang, T. Shao, M. Li, J. Gong, Bubble-supported engineering of hierarchical CuCo2S4 hollow spheres for enhanced electrochemical performance, J. Mater. Chem. A, 6 (2018) 5265-5270.
[44] Z. Liu, W. Zhou, S. Wang, W. Du, H. Zhang, C. Ding, Y. Du, L. Zhu, Facile synthesis of homogeneous core-shell Co3O4 mesoporous nanospheres as high performance electrode materials for supercapacitor, J. Alloy. Compd., 774 (2019) 137-144.
[45] J. Zhang, G. Zhang, W. Luo, Y. Sun, C. Jin, W. Zheng, Graphitic Carbon Coated CuO Hollow Nanospheres with Penetrated Mesochannels for High-Performance Asymmetric Supercapacitors, ACS Sustainable Chemistry & Engineering, 5 (2016) 105-111.
[46] M. Zeraati, K. Tahmasebi, Supercapacitor behavior of SiC coated copper hydroxide and copper sulfide nano-wires, J. Alloy. Compd., 786 (2019) 798-807.
[47] X. Zhang, L. Wei, X. Guo, Ultrathin mesoporous NiMoO4-modified MoO3 core/shell nanostructures: Enhanced capacitive storage and cycling performance for supercapacitors, Chem. Eng. J., 353 (2018) 615-625.
[48] Q. Zhang, H. Liu, Y. Xu, L. Wang, 3D nanoflower-like zinc hydroxyl carbonates for high performance asymmetric supercapacitors, J. Solid State Chem., 267 (2018) 76-84.
[49] Y. Liu, Z. Zhou, S. Zhang, W. Luo, G. Zhang, Controllable synthesis of CuS hollow microflowers hierarchical structures for asymmetric supercapacitors, Appl. Surf. Sci., 442 (2018) 711-719.
[50] A.A. Ensafi, H.A. Alinajafi, B. Rezaei, Adenine decorated@reduced graphene oxide, a new environmental friendly material for supercapacitor application, J. Alloy. Compd., 735 (2018) 1010-1016.
[51] Z. Qu, M. Shi, H. Wu, Y. Liu, J. Jiang, C. Yan, An efficient binder-free electrode with multiple carbonized channels wrapped by NiCo2O4 nanosheets for high-performance capacitive energy storage, J. Power Sources, 410-411 (2019) 179-187.
[52] Z. Gao, C. Chen, J. Chang, L. Chen, D. Wu, F. Xu, K. Jiang, Balanced energy density and power density: Asymmetric supercapacitor based on activated fullerene carbon soot anode and graphene-Co 3 O 4 composite cathode, Electrochim. Acta, 260 (2018) 932-943.
[53] S. Ramesh, D. Vikraman, H.-S. Kim, H.S. Kim, J.-H. Kim, Electrochemical performance of MWCNT/GO/NiCo2O4 decorated hybrid nanocomposite for supercapacitor electrode materials, J. Alloy. Compd., 765 (2018) 369-379.
[54] H. Liang, J. Lin, H. Jia, S. Chen, J. Qi, J. Cao, T. Lin, W. Fei, J. Feng, Hierarchical NiCo-

LDH@NiOOH core-shell heterostructure on carbon fiber cloth as battery-like electrode for supercapacitor, J. Power Sources, 378 (2018) 248-254.
[55] C.R. Rawool, S.P. Karna, A.K. Srivastava, Enhancing the supercapacitive performance of Nickel based metal organic framework-carbon nanofibers composite by changing the ligands, Electrochim. Acta, 294 (2019) 345-356.
[56] F. Wang, J. Zheng, G. Li, J. Ma, C. Yang, Q. Wang, Microwave synthesis of mesoporous CuCo 2 S 4 nanoparticles for supercapacitor applications, Mater. Chem. Phys., 215 (2018) 121-126.
[57] Y. Zhu, H. Chen, S. Chen, C. Li, M. Fan, K. Shu, Sea urchin-like architectures and nanowire arrays of cobalt–manganese sulfides for superior electrochemical energy storage performance, J. Mater. Sci., 53 (2018) 6157-6169.
[58] H. Wang, M. Liang, D. Duan, W. Shi, Y. Song, Z. Sun, Rose-like Ni 3 S 4 as battery-type electrode for hybrid supercapacitor with excellent charge storage performance, Chem. Eng. J., 350 (2018) 523-533.
[59] Y. Sui, H. Hu, J. Qi, Y. Zhou, F. Wei, Y. He, Q. Meng, Y. Ren, Z. Sun, Facile synthesis of Cu1.96S nanoparticles for enhanced energy density in flexible all-solid-state asymmetric supercapacitors, J. Mater. Sci-Mater. El, 29 (2018) 11187-11198.
[60] X. Han, K. Tao, D. Wang, L. Han, Design of a porous cobalt sulfide nanosheet array on Ni foam from zeolitic imidazolate frameworks as an advanced electrode for supercapacitors, Nanoscale, 10 (2018) 2735-2741.
[61] X. Yuan, B. Tang, Y. Sui, S. Huang, J. Qi, Y. Pu, F. Wei, Y. He, Q. Meng, P. Cao, CuCo2S4 nanotubes on carbon fiber papers for high-performance all-solid-state asymmetric supercapacitors, J. Mater. Sci-Mater. El, 29 (2018) 8636-8648.
[62] Q. Wang, X. Liang, D. Yang, D. Zhang, Facile synthesis of novel CuCo2S4 nanospheres for coaxial fiber supercapacitors, RSC Adv., 7 (2017) 29933-29937.
[63] X. Xu, Y. Liu, P. Dong, P.M. Ajayan, J. Shen, M. Ye, Mesostructured CuCo2S4/CuCo2O4 nanoflowers as advanced electrodes for asymmetric supercapacitors, J. Power Sources, 400 (2018) 96-103.